Remote Sensing of Environment 280 (2022) 113218

Contents lists available at ScienceDirect

Remote Sensing of Environment

journal homepage: www.elsevier.com/locate/rse

Analysis of regional large-gradient land subsidence in the Alto Guadalentín Basin (Spain) using open-access aerial LiDAR datasets

Liuru Hu [a,b,c], María I. Navarro-Hernández [a], Xiaojie Liu [a,d], Roberto Tomás [a,*], Xinming Tang [b], Guadalupe Bru [e], Pablo Ezquerro [e], Qingtao Zhang [f]

[a] Dpto. de Ingeniería Civil, Escuela Politécnica Superior de Alicante, Universidad de Alicante, P.O. Box 99, E-03080 Alicante, Spain
[b] Land Satellite Remote Sensing Application Center (LASAC), Ministry of Natural Resources of P.R. China, Beijing 100048, China
[c] The First Topographic Surveying Brigade of Ministry of Natural Resources of the People's Republic of China, Xi'an 710054, China
[d] School of Geological Engineering and Geomatics, Chang'an University, Xi'an 710054, China
[e] Geohazards InSAR Laboratory and Modeling Group (InSARlab), Geohazards and Climate Change Department, Geological Survey of Spain (IGME -CSIC), Calle de Ríos Rosas, 23, Madrid, Spain
[f] The First Geodetic Surveying Brigade of Ministry of Natural Resources of the People's Republic of China, Xi'an 710054, China

ARTICLE INFO

Editor: Jing M. Chen

Keywords:
Land subsidence
LiDAR
M3C2
InSAR
Cross-correlation analysis
Alto Guadalentín aquifer

ABSTRACT

Land subsidence associated with groundwater overexploitation in the Alto Guadalentín Basin (Spain) aquifer system has been detected during the last decades. In this work, for the first time, we propose a new point cloud differencing methodology to detect land subsidence at basin scale, based on the multiscale model-to-model cloud comparison (M3C2) algorithm. This method is applied to two open-access airborne LiDAR datasets acquired in 2009 and 2016, respectively. First the internal edge connection errors in the different flight lines were addressed by means of a smoothing point cloud method. LiDAR datasets capture information from ground and non-ground points. Therefore, a method combining gradient filtering and cloth simulation filtering (CSF) algorithms was applied to remove non-ground points. The iterative closest point (ICP) algorithm was used for point cloud registration of both point clouds exhibiting a very stable and robust performance. The results show that vertical deformation rates are up to −14 cm/year in the basin from 2009 to 2016, in agreement with the displacement reported by previous studies. LiDAR results have been compared to the velocity measured by continuous GNSS stations and an InSAR dataset. For the GNSS-LiDAR and InSAR-LiDAR comparison, we computed a common 100 × 100 m grid in order to assess any similarities and discrepancies. The results show a good agreement between the vertical displacements obtained from the three different surveying techniques. Furthermore, LiDAR results were compared with the distribution of compressible soil thickness showing a clear relationship. The study underlines the potential of open-access and non-customized LiDAR to monitor the distribution and magnitude of vertical deformations in areas prone to be affected by groundwater-withdrawal-induced land subsidence.

1. Introduction

The Alto Guadalentín valley is an intra-montane basin located in southeast Spain, filled by Neogene-Quaternary sediments, in which the build-up of alluvial deposits mostly comes from the transportation dynamics of the Guadalentín river (Béjar-Pizarro et al., 2016; Bonì et al., 2015). The basin contains a multi-layer aquifer system covering an area of approximately 277 km^2, subjected to water abstractions during the past 50 years. The development of the agriculture industry and the accelerated population growth triggered the reduction of the piezometric levels, which have reached >200 m of drop (Béjar-Pizarro et al., 2016; Bonì et al., 2015; Rigo et al., 2013). Groundwater withdrawal reduces pore water pressure in voids between soil particles (Balasubramaniam and Brenner, 1981). As a consequence, the effective stress on soil increases, resulting in a gradual compaction of the sediments that causes the lowering of the ground surface (González and Fernández, 2011).

During the last decades, interferometric synthetic aperture radar (InSAR) has become a widespread technique for monitoring land subsidence induced by groundwater extraction in the Alto Guadalentín basin (Béjar-Pizarro et al., 2016; Bonì et al., 2015; Ezquerro et al., 2017; Ezquerro et al., 2020; Fernandez et al., 2018; González and Fernandez,

* Corresponding author.
E-mail address: roberto.tomas@ua.es (R. Tomás).

https://doi.org/10.1016/j.rse.2022.113218
Received 12 March 2022; Received in revised form 29 July 2022; Accepted 7 August 2022

2011; González and Fernández, 2011; Rigo et al., 2013). Previous studies based on multi-satellites SAR (Synthetic Aperture Radar) observations revealed that the maximum deformation area of the basin reached vertical rates of −10 cm/year between 1992 and 2007 (Bonì et al., 2015), of −11 cm/year between 2011 and 2016, and of −9.7 cm/year between 2014 and 2016, showing a displacement velocity decrease in the later period (Ezquerro et al., 2020). Remote sensing techniques provide a high density of land surface displacement measurements across large areas at a relative low-cost in comparison with conventional ground-based technique (Tomás et al., 2013), also enabling the analysis of the spatial distribution and the evolution of the displacements (Amighpey and Arabi, 2016; Béjar-Pizarro et al., 2016; Castellazzi et al., 2016; Galloway and Hoffmann, 2007; Ge et al., 2014; Hu et al., 2019; Tomás et al., 2005; Yousefi and Talebbeydokhti, 2021).

However, previous studies have monitored groundwater-withdrawal-induced land subsidence only using InSAR, leveling and GNSS remote sensing techniques. As a consequence, several challenges have arisen for detailed land subsidence investigations by means of InSAR for the following reasons: (1) temporal decorrelation, which causes the loss of coherence due to changes in surface cover and the absence of ability for directly calculate the deformation using two long time interval datasets (Sansosti et al., 2014); (2) geometrical decorrelation, which causes the loss of coherence in areas with steep terrain and dense vegetation due to the variation of the observed angle for each resolution cell between the two acquisitions (Vajedian et al., 2015); (3) atmospheric artifacts, which are one of the major error sources in InSAR due to spatial and temporal variations of tropospheric delays (Bekaert et al., 2015b; Xiao et al., 2021). It is worth noting that in previously published works, aerial LiDAR datasets are used as auxiliary information for InSAR processing (He et al., 2021; Khan et al., 2014) or for change detection of small areas (Bernard et al., 2021; Imakiire and Koarai, 2012; Koning et al., 2020; Scott et al., 2021). However, the main novelty of this paper is the solution developed for the evaluation of vertical deformations caused by groundwater-withdrawal-induced land subsidence at wide-spread scale, based on open-access, non-specifically acquired and non-customized LiDAR point clouds.

Therefore, the main objective of this study was to propose a new flowchart to measure groundwater-withdrawal-induced land subsidence using wide-spread and multi-temporal open-access point cloud datasets. We illustrated the uncertainty of working directly on open-access and non-specifically acquired point clouds to generate a land subsidence cumulative map. Also, we discussed the methodological advantages of direct operating on point clouds, in terms of comparing with InSAR. In previous studies, topographic differences detected by LiDAR technique allowed to measure ground surface changes caused by earthquakes (Borsa and Minster, 2012; Scott et al., 2019), coastal process (Brock et al., 2001; Bull et al., 2010) and landslides (Bernard et al., 2021), among other events (Scott et al., 2021). With this aim, Lague et al. (2013) implemented the multiscale model-to-model cloud comparison (M3C2) algorithm. It considers a direct point cloud comparison by measuring the accurate orthogonal distance between two point clouds datasets acquired at different times in three-dimensions (3D). This algorithm has been broadly used for geomorphological change detection of landslides (Bernard et al., 2021; Scott et al., 2021).

The paper is organized as follows: in Section 2, the LiDAR dataset and other data collected are presented, followed by a detailed description of the LiDAR processing in Section 3. Then, in Sections 4 and 5, the use of LiDAR, together with InSAR and GNSS, have enabled the detection of surface movements and the assessment of correlations to verify the precision of the proposed approach. Subsequently, the deformation results from LiDAR, InSAR and GNSS stations, have been compared with the spatial distribution of compressible soil thickness. Finally, in Section 6, in light of the results, the advantages and limitations of LiDAR technique for measuring land subsidence were discussed in comparison with InSAR.

2. Study area and datasets

2.1. Study area

The Alto Guadalentín valley is an elongated ENE-WSW oriented intramontane basin of the Betic range located in the Murcia Province, SE Spain (Silva, 2014) (Fig. 1a). The valley develops in a tectonic depression up to 1000 m depth that exhibits a horst and graben structure (Cerón and Pulido, 1996). This is a seismically active area bordered to the north by the Alhama de Murcia fault (Fig. 1a), one of the more prominent active faults of SE Spain (Martinez-Diaz et al., 2012). Some alluvial fans develop on NW reliefs intersecting the deposits of the valley (Fig. 1a). The valley is delimited by mountain ranges mainly made of metamorphic rocks, carbonates, sandstones and conglomerates (IGME, 1981) (Fig. 1a) that reach elevations up to 927 and 597 m a.s.l. at NW and SE, respectively. The depression is filled by Neogene-Quaternary unconsolidated sediments deposited by the Guadalentín river (Cerón and Pulido, 1996), that drains the basin. Bonì et al. (2015) calculated the distribution of compressible soil thickness of the finer fraction of the Neogene-Quaternary filling (i.e. the silt and clay of the more compressible layers) from 23 boreholes, then updated by Béjar-Pizarro et al. (2016) using InSAR and GNSS data to obtain the map shown in Fig. 1b.

The substrata of the tectonic depression is made of metamorphic rocks that outcrop on the edges of the basin. On the top of this unit, there are Tertiary marls that constitute the impervious bottom of the aquifer system, reaching thicknesses varying from 300 to 900 m due to the strong control exercised by the horst and graben structure (Cerón García, 1995; IGME, 1981). The main aquifer is composed by the topmost unconsolidated Plio-Quaternary sediments mainly made of sand and gravel layers interbedded with silt and clayey layers.

The area presents a semi-arid climate with annual accumulated rainfall of 250 mm characterized by the presence of yearly pronounced dry periods. The valley floodplain is intensively cultivated using groundwater resources from the underlying aquifer system. The increasing groundwater extraction from the 60s to the 80s led to the overexploitation of the aquifer that was declared officially overexploited in 1987 (CHS, 2006). Later, the Tajus-Segura diversion slightly alleviated the situation, reducing groundwater extraction in some areas in which the piezometric levels stabilized. However, the pumping of groundwater continued in the NW and N sectors of the valley (nearby the city of Lorca that has a population of over 90,000 inhabitants) inducing groundwater level declines over 200 m between 1960 and 2012 (Ezquerro et al., 2017). Although the piezometric level remained mostly stable during the last few years, the phenomenon of land subsidence continues due the existing time delay because of the gradual transfer of stress from the pore pressure to the effective stress. As a consequence, land subsidence occurred in this area at a rate over 11 cm/year (Béjar-Pizarro et al., 2016; Bonì et al., 2015; Ezquerro et al., 2017; Ezquerro et al., 2020; Fernandez et al., 2018; González and Fernández, 2011) being the greatest in Europe caused by groundwater withdrawal.

2.2. Datasets

2.2.1. LiDAR

The LiDAR (Light Detection and Ranging) point cloud datasets used in this work were downloaded from the Geoportal web of the National Plan for Aerial Orthophotography (PNOA) of Spain, a nation-wide project of LiDAR flights for massive production of point clouds. These datasets are freely available, covering the whole national territory (CNIG, 2022). The geodetic reference system of the point cloud is ETRS89 compatible with WGS84, the projection is Universal Transverse Mercator (UTM) in the spindle zone corresponding to each file and the altitudes are in orthometric heights.

The point clouds were captured with a density of 0.5 points/m^2 according to the technical specifications of the flight. Afterward, these

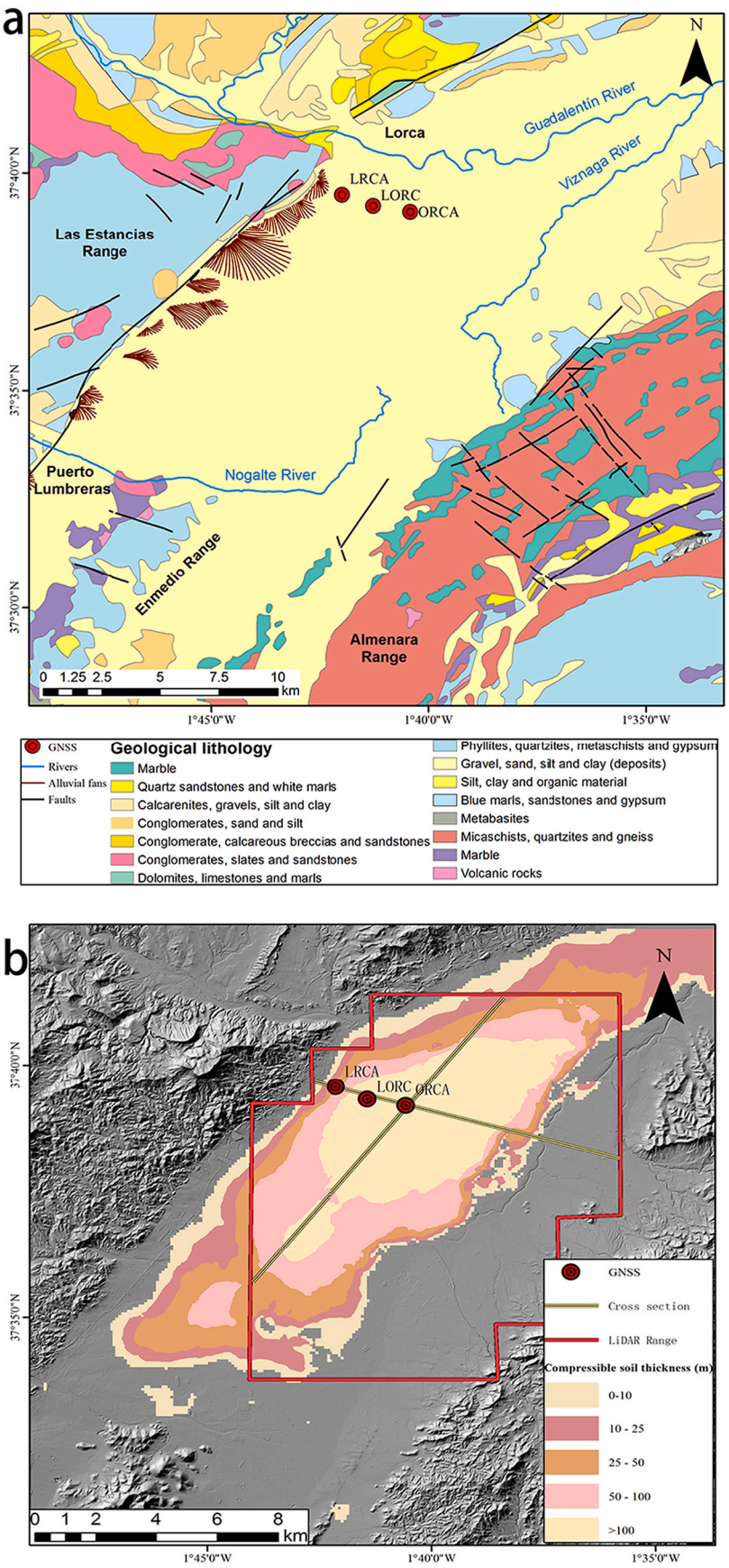

Fig. 1. (a) Geological setting of the Alto Guadalentín Basin modified from IGME (1981). Permanent GNSS stations LRCA, LORC and ORCA are also shown. (b) Compressible soil thickness distribution. The thickness of the compressible deposits has been calculated by means of geotechnical borehole data from Bonì et al. (2015) and Béjar-Pizarro et al. (2016).

point clouds were automatically classified and colored by RGB (red, green and blue) obtained from orthophotos of the PNOA with a pixel size of 25 or 50 cm (Monterroso Checa, 2017). The main characteristics of the point clouds used in this work are summarized in Table 1.

Although the required height accuracy of LiDAR was 0.4 and 0.2 m in 2009 and 2016 respectively, the real height accuracy is higher. From the altimetric precision control information of each independent point cloud provided by the IGN, the average relative flight heights were 2727 and 3317 m, the minimum and maximum pulse rates vary from 70.2 and 89.2 kHz, and 74.8 and 89.2 kHz, respectively. Additionally, the real height accuracies evaluated by means of the RMSE comparing reference benchmarks located on the ground by determining the corresponding Euclidean distance between the checkpoints and the point clouds were 0.113 and 0.083 m for the datasets of 2009 and 2016, respectively (IGN, 2009; IGN, 2016). Consequently, the estimated error for the differences calculated between both point clouds can be evaluated as the propagation of the errors providing a RMSE value of 0.140 m and 0.020 m/year for the absolute subsidence and the deformation rate, respectively. The estimated error is a lower estimation from the RMSE. Obviously, the actual error will be higher since the processing error should be included. However, the flight line, the filtering and the registration errors are difficult to be evaluated (Lague et al., 2013).

2.2.2. InSAR

To test the agreement between the temporal evolution of ground surface displacement obtained by LiDAR and previous InSAR studies, the results from 114 X-band SAR images acquired by Cosmo-SkyMed (hereinafter referred to as CSK) satellites were used (Ezquerro et al., 2020). The CSK dataset covers the time period from June 2011 to December 2016 in an ascending orbit direction and an area of 676 km^2, with maximum temporal and spatial baseline of 269 days and 488 m, respectively, in order to reduce temporal decorrelation.

Due to the agricultural predominance of the processed area, a Small Baselines (SBAS) approach was selected to ensure a good point density. The advanced differential SAR interferometry algorithm Coherent Pixels Technique (CPT) (Blanco-Sánchez et al., 2008), a Persistent Scatterer Interferometry technique, was used to generate line of sight (LOS) displacement time series. This algorithm is characterized by the capability to isolate the atmospheric artifacts component and to minimize the noise contribution enabling an accurate estimation of the displacements. The obtained displacements maps contained 422,458 coherent pixels with a resolution near 25 × 25 m selected according to their coherence (higher than 0.40). For further details on the processing of SAR data we refer the reader to the work published by Ezquerro et al. (2020).

2.2.3. GNSS

Three permanent Global Navigation Satellite System (GNSS) stations named LRCA, LORC and ORCA (Fig. 1) are located in the north-western sector of the study area (Bonì et al., 2015; Ezquerro et al., 2020).

ORCA GNSS station (Fig. 1) is placed in the area of maximum subsidence providing information from February 2016 to September 2017 (Fernández-Merodo et al., 2021). The LRCA dataset covers the period December 2012 – September 2017, while LORC dataset spans from April 2011 to September 2017. Daily GNSS stations measurements are weekly processed by the IGN using the software Bernese 5.2 (Dach et al., 2015).

3. Methodology

A new approach to monitor land subsidence using LiDAR point clouds is presented in this section. Fig. 2 shows the workflow and the main modules of the approach, which can be organized into four steps as

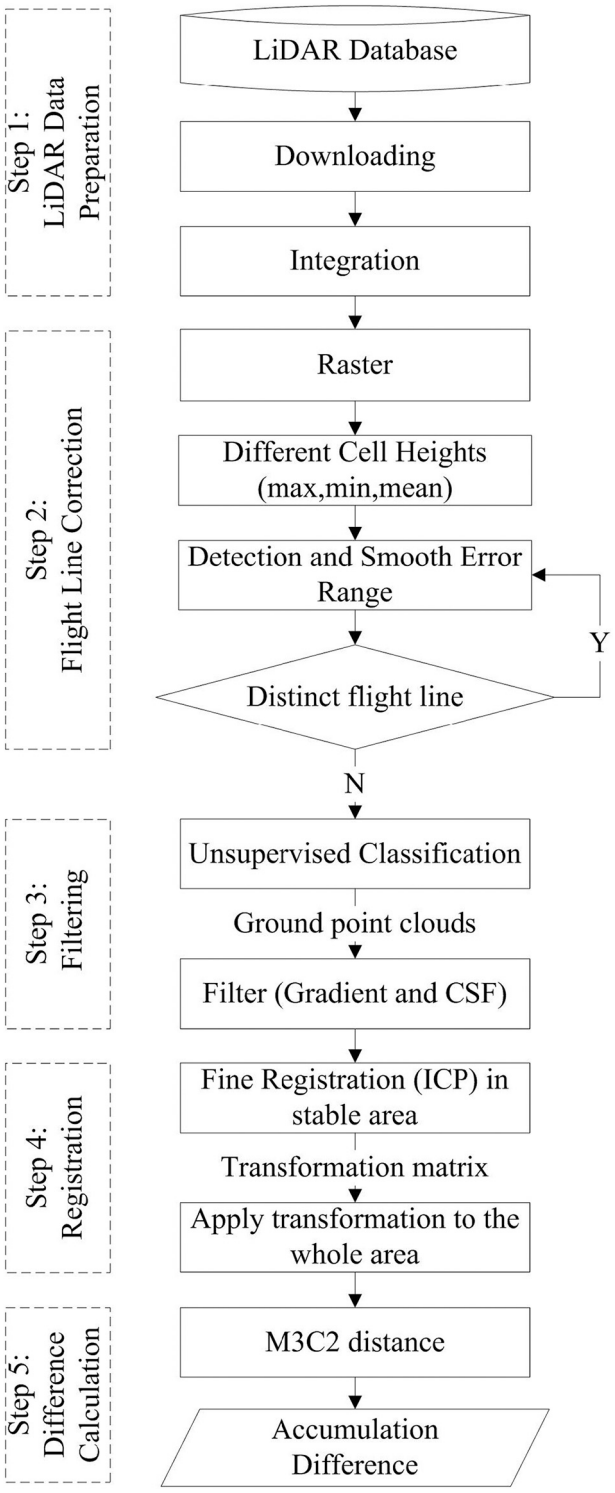

Fig. 2. Flowchart of the LiDAR data processing used in this work.

Table 1
Basic parameters of the LiDAR datasets from Lorca used in this study (IGN, 2022).

Processing year	Flight start date (yyyy/mm)	Flight end date (yyyy/mm)	Density (p/m^2)	Flight relative height (m)	Pulse rate (kHz)	RMSE z (m)	Main sensor
2009	2009/10	2009/11	0.5	2727	70.2/89.2	0.113	LEICA ALS50
2016	2016/08	2016/09	0.5	3317	74.8/89.2	0.083	LEICA ALS60

follows.

Step 1: First, the point clouds were downloaded from the IGN server. Each point cloud dataset was independently processed performing its integration and merging.

Step 2: Because of internal elevation edge connection errors and adjacent edge strips misplaced, the point cloud elevation errors are significant in the different flight strips. To detect and smooth the error range, the first step consisted in separating the filtered point clouds into different cell heights (i.e. maximum, minimum and mean cell heights). To this aim, a raster grid was generated and the maximum, minimum and mean heights values were calculated for each cell. Regarding the calculation of the mean cell height of every cell, the median point was chosen if the cell contained an odd number of points, otherwise the point with the closest value to the average was selected for an even number of points. As the density of point clouds is 0.5 p/m^2, a 2 m raster grid range was selected. At this point, rasterization effectively improved the distribution of point clouds on the datasets which was originally irregular and unstructured, taking up huge storage space. Then, the mean cell height was adopted as default value for each pixel of the rasterized point clouds. However, since a clear strip pattern was still observed along the distinct flight lines, the mean height values in the flight lines were replaced by smoother values derived from the maximum and minimum cell heights. To this aim, the M3C2 calculation which was comprehensively discussed in Step 5 was used to identify the cell height values from the maximum and minimum rasterized point clouds that minimize the differences between 2009 and 2016 rasterized point clouds as follows. Firstly, the M3C2 distances between the maximum height values of each rasterized point cloud (i.e. 2009 and 2016) were calculated. Secondly, the same distances were calculated for the minimum height values of each rasterized point clouds. Finally, comparing the M3C2 differences on both sides of the flight lines from both rasterized point clouds, the height values that exhibited minimal M3C2 differences were adopted to replace the mean height values in the flight lines in order to be used in the next steps.

Step 3: The rasterized point clouds were filtered in order to separate them into ground and non-ground points. This is an essential and preliminary step to detect ground deformations. Otherwise, the real deformations would be hidden by non-ground (i.e. man-made) change noise. Therefore, firstly, the rasterized point clouds were separated into ground and non-ground points by means of the "Classify LAS ground" tool in ArcGIS (ArcGIS, 2022) selecting a conservative ground detection method to identify ground points. Then the classified ground points with great gradient were judged by the gradient algorithm, which removed non-ground points preserving ground points to a great degree (Li, 2013). Subsequently, we filtered dense and continuous non-ground points using the cloth simulation filter (CSF) algorithm (Zhang et al., 2016) which considers terrain as a piece of cloth sticking to the surface in which the shape of the cloth is the Digital Surface Model (DSM). Second, the point cloud is turned upside down, and then the surface of the cloth is the Digital Elevation Model (DEM). Finally, based on the cloth simulation technique, we utilized CSF algorithm to extract wide-spread non-ground points from LiDAR point cloud. In this way, the original DSM is transformed into a DEM. It should be noted that the successive application of the CSF algorithm jointly with the unsupervised classification and gradient algorithms ensures a conservative estimation of ground points in order to reduce the noise (Cai et al., 2019; Zhang et al., 2016).

Step 4: The iterative closest point (ICP) algorithm is used for the registration of the rasterized point cloud to perform a robust alignment. The selection of the ICP is based on the stability and robustness of this algorithm to perform the rigid transformation that enables translating and rotating the point cloud while maintaining their shape and scale (Li et al., 2020; Wang et al., 2020). It should be noted that this transformation has six degrees of freedom (3 for translation and 3 for rotation). Therefore, the registration precision is affected by the subsidence area. In this case, the point clouds were firstly aligned in the stable area by ICP to gain the transformation matrix. The oldest Permian-Triassic mountain areas that run parallel to the valley direction were considered as stable areas based on geological criteria, and in agreement with the stable areas shown by InSAR results. Then the whole point clouds were aligned by using the transformation matrix obtained in the previous step.

Step 5: The deformation between two epochs was vertically estimated on point clouds without the need for surface interpolation or gridding, by means of the multiscale model-to-model cloud comparison (M3C2) algorithm (Bernard et al., 2021). M3C2 enables the estimation of orthogonal distances in a multi-temporal airborne LiDAR dataset. In the M3C2 algorithm, assuming two successive point clouds, the first one will be called the reference point cloud, and the second one the comparison point cloud. While M3C2 can be applied on all points, the reference point cloud is taken as the core point in this work. The use of a regular grid of core points is not only to allow the computation of robust statistics of changes unbiased by spatial variations in point density, but also to speed up calculation. Finally, the aligned dataset was calculated by M3C2, and the cumulative difference was obtained.

Finally, InSAR and LiDAR results were homogenized, with the aim of comparing them to evaluate their correlation and differences. Firstly, the velocity and the cumulative InSAR displacements measured along the line of sight (LOS) of the satellite were projected along the vertical direction considering the acquisition angle of InSAR to make them comparable. Then, we tessellated the common subsidence area between InSAR and LiDAR datasets using squares of 100 m of side. Finally, we calculated the mean values for each grid to compare and correlate both datasets.

Additionally, the vertical displacement rates including InSAR and LiDAR along two cross-sections passing through the GNSS stations have been also compared to assess the accuracy of the results. In order to do so, all points contained within a 10 m buffer area around the profiles were selected for plotting the cross sections. The GNSS vertical velocities and the compressible soil thickness derived from Fig. 1b were also represented on the profiles. Finally, the maximum discrepancy (MaxD), the minimum discrepancy (MinD), the mean absolute discrepancy (MD), the standard deviation of the discrepancy, the root mean square error (RMSE) and the mean absolute percentage error (MAPE) between GNSS, LiDAR and InSAR were calculated for LORC and ORCA GNSS stations.

4. Results and analyses

4.1. LiDAR results

Fig. 3a shows the velocity results calculated by the proposed LiDAR-based method over the study area, covering an extension of about 140 km^2. As can be seen, although the distinct adjacent flight lines have been processed, the results show a clear strip pattern. These height "steps" are related to the discrepancies between overlapping LiDAR strips (Latypov, 2002; Zhang et al., 2015) of the different flight lines (Fig. S1).

The results show that maximum cumulative displacements derived from LiDAR reached up to −98 cm, corresponding to an annual velocity of −14 cm/year. The areas with the highest subsidence rates (i.e. faster than −7 cm/year) exhibit a SW-NE elliptical shape parallel to the valley direction located in the central sector of the Alto Guadalentín Basin (Fig. 3a). Note that areas affected by severe subsidence cover 20.55 km^2, while stable areas exhibiting displacement rates between −1 and 1 cm/year occupy only 29.89 km^2 as shown in Table 2. It is worth noting that there are some uplifting zones within the study area covering an extension of 20.98 km^2 probably related to the accuracy of LiDAR and the processing errors.

4.2. Comparison with InSAR time series

In this section, the calculated LiDAR results and measurements derived from InSAR data are compared (Fig. 3a-b). We have used the same colour scale for both figures for direct comparison purposes,

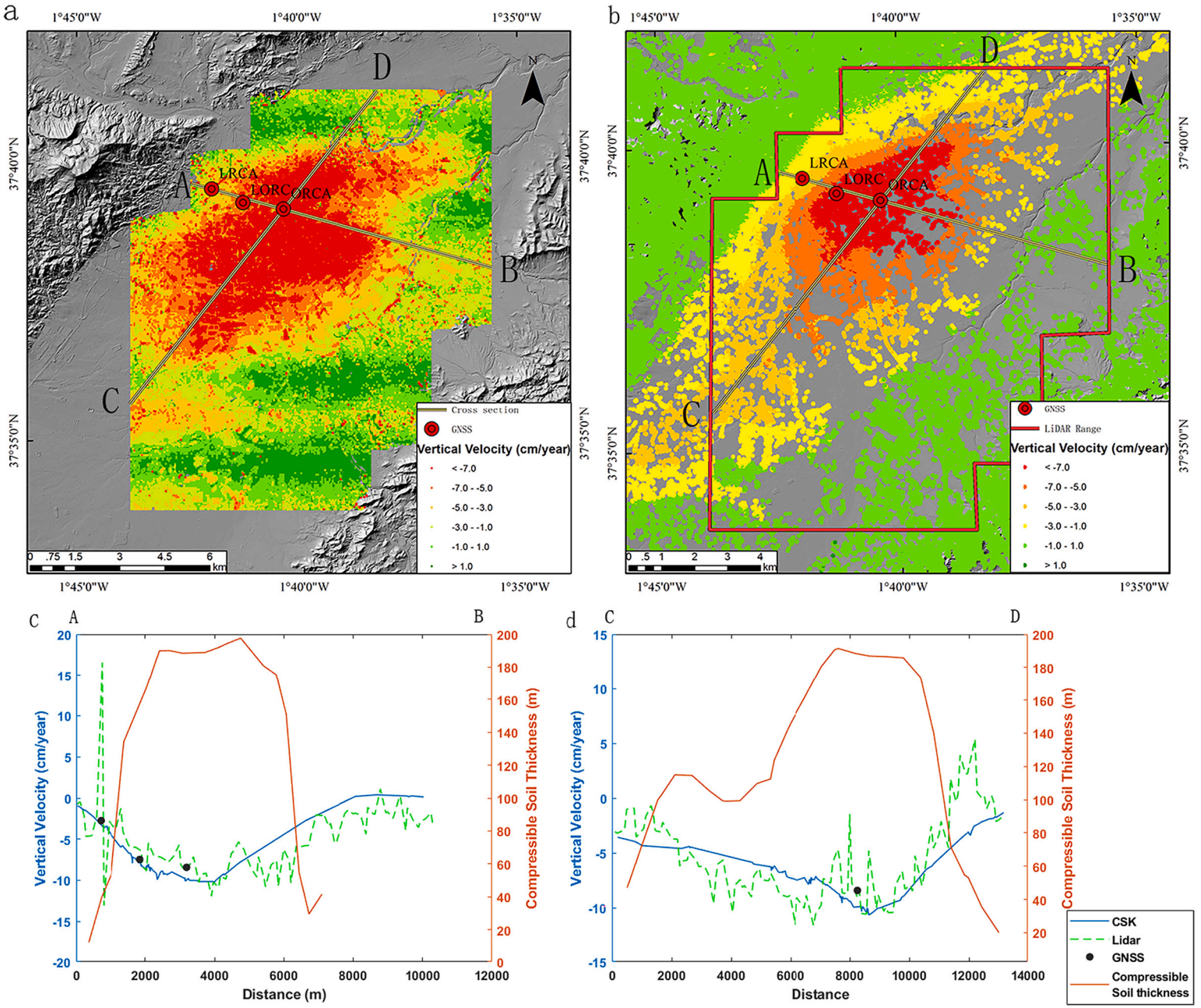

Fig. 3. (a) Vertical velocity map for the 2009–2016 period derived from LiDAR data. (b) Vertical velocity maps for the 2011–2016 period obtained from COSMO-SkyMed satellites. (c) and (d) Cross-sections showing the vertical ground deformation rates derived from LiDAR (green dotted lines), InSAR (blue lines), GNSS (black dots), and compressible soil thickness (red lines). The location of the cross-sections A-B, C—D is shown in (a). (For interpretation of the references to colour in this figure legend, the reader is referred to the web version of this article.)

Table 2
Distribution of areas affected by subsidence rate for LiDAR and InSAR results.

Subsidence interval (cm/year)	Subsiding area from LiDAR (km^2)	Subsiding area from InSAR (km^2)	Difference (km^2)
<−7	20.55	11.05	9.50
−7 to −5	16.49	16.97	0.48
−5 to −3	20.77	26.99	6.22
−3 to −1	28.98	28.36	0.62
−1 to 1	29.89	54.29	24.40
>1	20.98	0.00	20.98

adopting velocities in the range of ±1 cm/year as stable, as adopted for InSAR datasets in this area by other authors. The highest land subsidence areas derived from InSAR (Fig. 3b) show a similar shape and distribution than LiDAR results (Fig. 3a). Comparing these two patterns (Fig. 3a and b), InSAR shows a larger subsidence bowl and a more obvious trend parallel to the valley direction. However, the spatial extent of the highest subsidence areas is different, reducing from 20.55 km^2 in LiDAR results to 11.05 km^2 in InSAR (Table 2), with a difference of 9.50 km^2. Areas between −7 to −5 cm/year and − 3 to −1 cm/year thresholds in LiDAR are similar to that defined by InSAR results, but the uplift area (> 1 cm/year) and the stable area (−1 to 1 cm/year) increase the difference to 20.98 km^2 and 24.40 km^2 between them as shown in Table 2. The potential reason is the different sensitivity between LiDAR and InSAR technologies in stable areas, especially in the region of change, as well as the potential errors inherent to the processing of the LiDAR data (e.g. the removal of the non-ground points from the original point clouds).

Fig. 4a shows the correlation between the displacements obtained from LiDAR and InSAR data. The Pearson (R) and Spearman (Rs) correlation coefficients reach values of 0.7002 and 0.6842. The difference between both coefficients are because Rs evaluates their degree of monotonicity and R measures the degree of linearity between two vectors of data (De Winter et al., 2016). It should be noted that R is more sensitive to outliers than Rs. The histogram and spatial distribution of differences between LiDAR and InSAR measurements is depicted in Fig. 4b, c and d. As it can be seen, the differences between LiDAR and InSAR vertical displacement rates are normally distributed, with an average difference of −0.49 cm/year, standard deviation of 1.80 cm/year and maximum and minimum differences of 8.05 cm/year and − 13.15 cm/year, respectively. The analysis performed in these sections confirms the reliability of aerial LiDAR datasets to obtain land subsidence rate maps in wide areas by means of the proposed methodology.

4.3. Comparison between LiDAR and GNSS time series

Continuous GNSS permanent stations (see the aerial surroundings in Fig. 5) grant checkpoints to validate the LiDAR and InSAR results. Fig. 6 and Table 3 show the inter-comparison of the time series obtained by the three techniques used in this paper (i.e. LiDAR, InSAR and GNSS) and the corresponding statistics for ORCA and LORC stations. The analysis of aerial orthophotos over time allows an assessment of changes on urban morphology or land cover (Fig. 5) and shows that the surroundings of LRCA station changed dramatically between 2009 and 2013. Consequently, only LORC and ORCA were used for the validation and the analysis of the subsequent results. The statistics of the comparison between LiDAR and GNSS is minimum (Table 3). The discrepancy between LiDAR and GNSS can be observed that MaxD is 0.584 cm/year, and MinD is 0.385 cm/year, and MD is 0.484 cm/year, and the standard deviation of discrepancy is 0.141 cm/year, and RMSE is 0.494 cm/year, and MAPE is 6.618%.

The surrounding area of LRCA station was fully rebuilt between 2009 and 2011, creating new man-made features, during the period only covered by LiDAR (Fig. 5a-b). In contrast, there were relatively few changes at LRCA station from 2011 to 2016, which was the period covered by LiDAR, InSAR and GNSS (Fig. 5b-d). Therefore, due to the relative stability of the region in which LRCA station is located, the influence of the variation of man-made features is much higher than the subsidence caused by groundwater withdrawal (Fig. 5m-p). To illustrate this interpretation, we have added the DSMs derived from LiDAR in 2009 and in 2016. Additionally, we have overlapped the LiDAR and InSAR vertical velocity results in LRCA station (Fig. 5m-p). Consequently, it is reasonable to believe that LiDAR-derived displacements show an opposite trend (i.e. uplift of up to 8.66 cm/year) compared with InSAR and GNSS (Fig. 6a). In contrast, the displacements measured by InSAR and GNSS exhibit very similar trends with displacement rates of −3.40 and − 2.75 cm/year, respectively.

LORC GNSS station time series available for this study are the longest of all available GNSS datasets. In this location GNSS, InSAR and LiDAR velocities are −7.46, −8.10 and − 6.58 cm/year, respectively, showing a consistent trend between the three techniques with a higher coincidence between InSAR and GNSS (Fig. 6b).

ORCA station shows the highest detected velocities, −8.42 cm/year, while InSAR and LiDAR velocities at that point are −9.96 and − 7.50 cm/year, respectively. It should be mentioned that, even if ORCA station time series is the shortest, only covering the two year period, LiDAR velocity matches well GNSS time series (Fig. 6c). InSAR time series are steeper than LiDAR and GNSS results, although they also exhibit a similar trend in the stations (Fig. 6c).

4.4. Comparison between LiDAR results and compressible soil thickness

As previously mentioned, the spatial distribution of land subsidence matches with the distribution of Plio-Quaternary unconsolidated compressible materials (i.e. silts and clays). Compressible soil thicknesses >100 m are located in the central part of the basin, whereas the bordering areas of the basin present thinner compressible soils layers (Fig. 1b). The relationship between compressible soil thickness and subsidence rates estimated from LiDAR in the studied area is straightforward as shown in Fig. 7a. This figure shows, as it was expected, that the maximum subsidence rates are measured on the thickest compressible soils area, and the trend of the boxplot statistic distribution decreases as the thickness increases. Subsidence rate varies in the range − 37 to 14 cm/year and − 9 to 37 cm/year for compressible soil thickness varying from 0 to 10 m and > 100 m, respectively. The observed outlier values are mainly related to the change caused by the features built between both LiDAR flights performed in 2009 and 2016 not filtered during step 3 of the processing algorithm that introduce apparent displacements of ground surface. InSAR displacement rates also show a clear relationship with the spatial distribution of compressible soil thickness in Fig. 7b. The comparison between soil thickness and vertical InSAR deformation rates shows a similar trend. Subsidence rate varies in the range − 4.23 to 0.48 cm/year and − 11.17 to −3.02 cm/year for compressible soil thickness varying from 0 to 10 m and > 100 m, respectively.

As can be seen, the distribution of the compressible deposit controls the magnitude of the deformation. Therefore, the thicker the accumulated compressible soil thickness the larger the subsidence magnitude. The above described relationship can be observed along cross sections A-B and C—D, plotted in Fig. 3c-d as well as in Fig. 7. A good agreement is also observed among land subsidence measured by means of the three techniques.

5. Discussion

5.1. Sources of uncertainty in LiDAR process

Identifying the sources of uncertainty in point cloud process is essential to improve the accuracy and efficiency of the proposed methodology. Three main uncertain sources can be identified.

The first one is related to the cell height uncertainty of the point clouds. In order to filter the flight line errors, the raw point clouds of

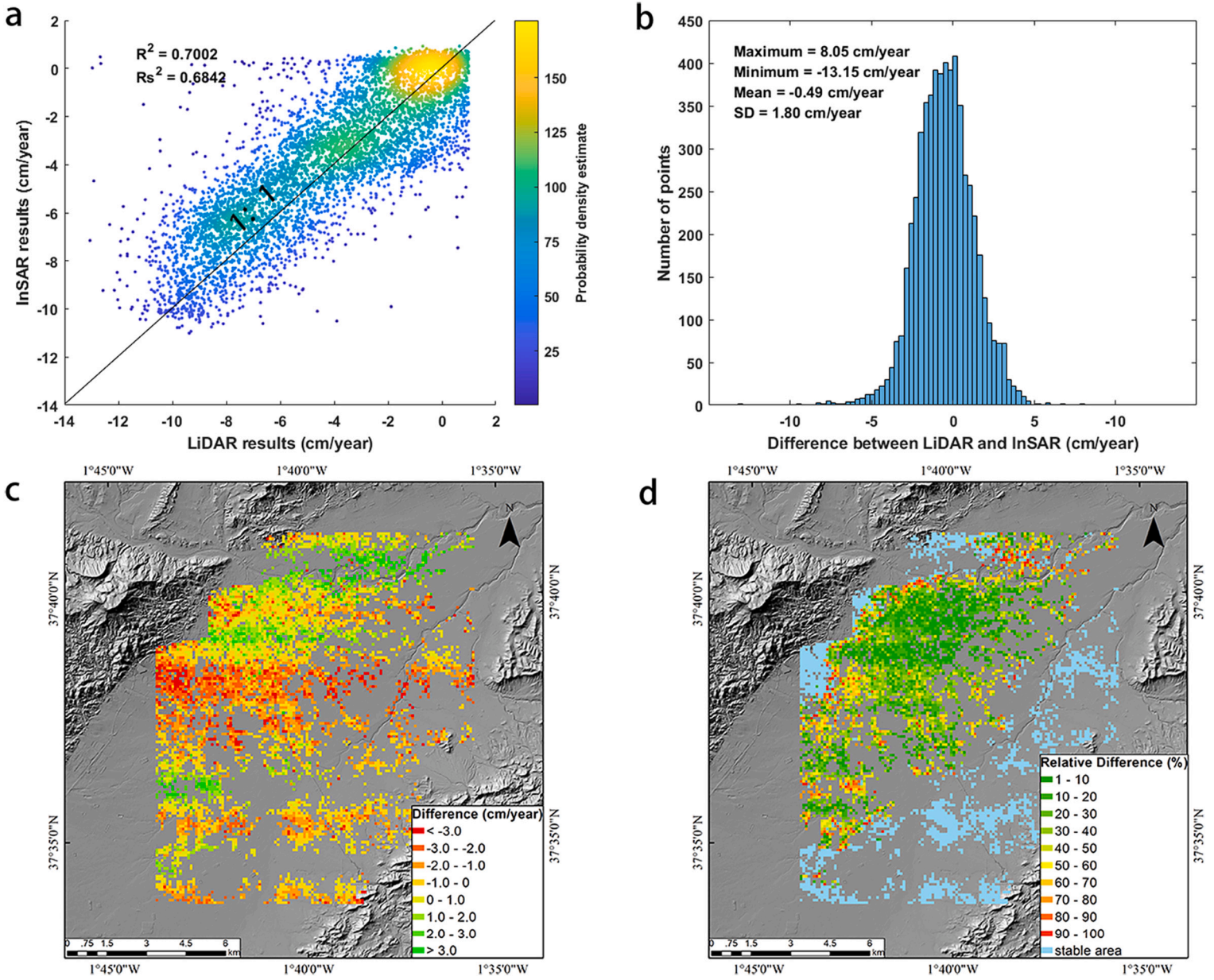

Fig. 4. (a) Correlation and (b) differences between LiDAR and InSAR data projected in the vertical direction. Rs and R are the Spearman and Pearson correlation coefficient, respectively. (c) Spatial difference map between LiDAR and InSAR. (d) Spatial relative difference map between LiDAR and InSAR. Note that positive and negative values in b and c indicate an overestimation and an underestimation, respectively, of the displacements measured by LiDAR. The stable areas in d have been masked out in order to avoid the overvaluation of the relative differences.

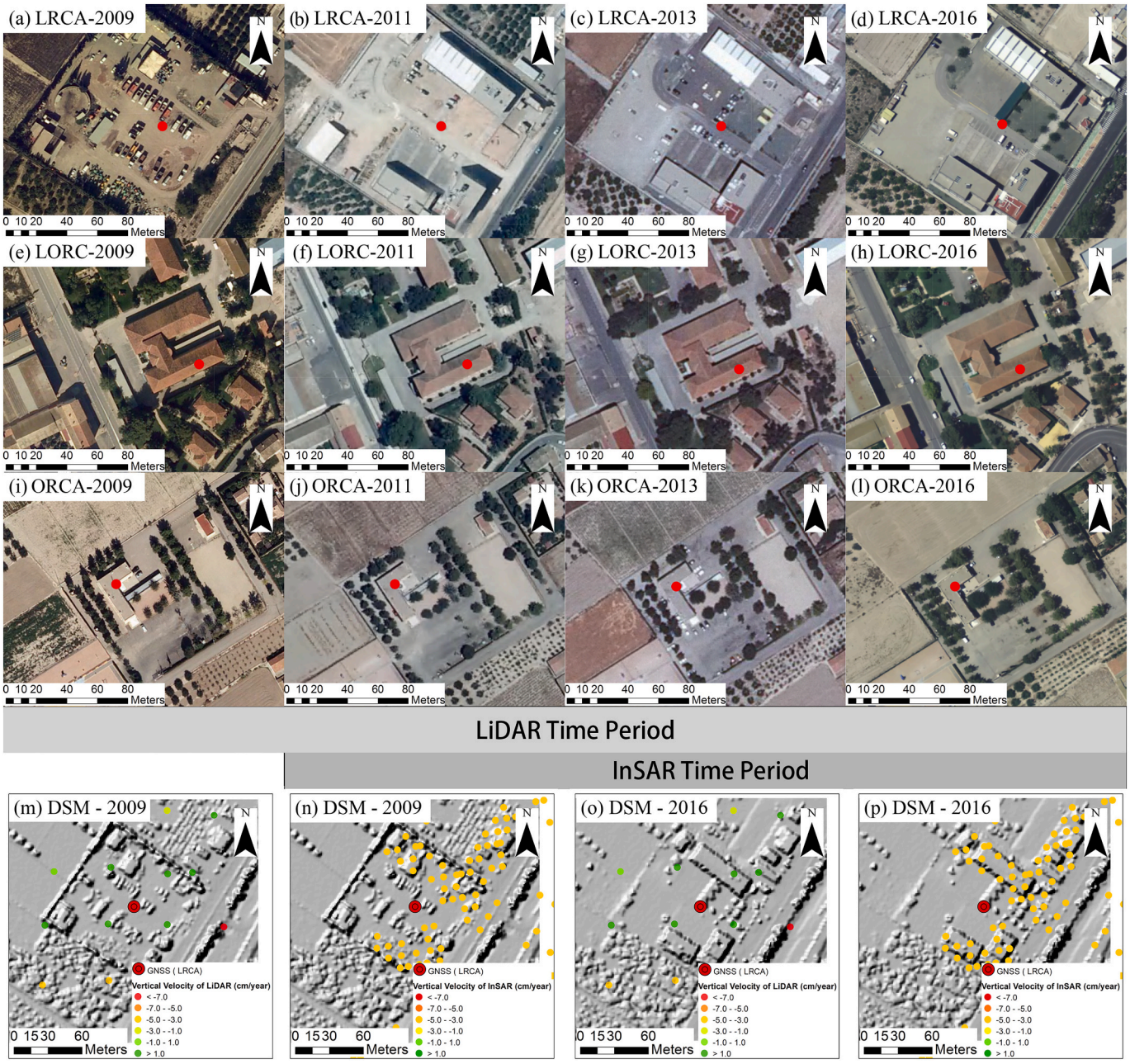

Fig. 5. Aerial view of GNSS stations over time (GeaMap, 2022). The GNSS stations have been labelled using red points. (m-p) DSM derived from LiDAR of 2009 and 2016 in LRCA station overlapping with LiDAR and InSAR vertical velocity results. (For interpretation of the references to colour in this figure legend, the reader is referred to the web version of this article.)

smooth parts among the three different cell height (i.e. the mean, maximum and minimum cell heights) is irregular and unstructured. Moreover, open-access and non-customized (i.e. non-specifically acquired) pre-processed point clouds have been used, instead of raw data acquired ad-hoc. It makes it hard to separate the datasets from different flight lines. Hence, there is a high probability that the distances between the compared point clouds contain points of different flights that leads to the comparison of different cell heights. Furthermore, GNSS and LiDAR in the study area are in different elevation coordinate systems, and it is difficult to gain the high-accuracy correction data between geodetic height and normal height. Consequently, there are no GCPs (ground control points) to be used to evaluate the accuracy of different cell heights.

The second source of uncertainty is due to the residual non-ground points. The residual number and the rejection rate of points after the application of different filtering processes is shown in Table 4. Due to the properties of the distinct filters, the advantage of the successive application of filters is obvious (Cai et al., 2019; Zhang et al., 2016). Since there is no benchmark datasets, the rejection error (i.e. the misclassified ground points as non-ground points), the acceptance error (i.e. the misclassification of non-ground points as ground points), and the total error (i.e. the proportion of all the misclassified points out of all points), are impossible to be calculated (Chen et al., 2021; Chen et al., 2013; Deng et al., 2021; Li et al., 2017). Therefore, some residual non-ground points may still remain in the point clouds after the filtering process influencing the M3C2 results and distorting the determination of the land subsidence magnitude.

Another source of error is the uncertainty in point cloud comparison (Lague et al., 2013). On the one hand, the position of point clouds not only depends on distance from the sensor to the surface and the

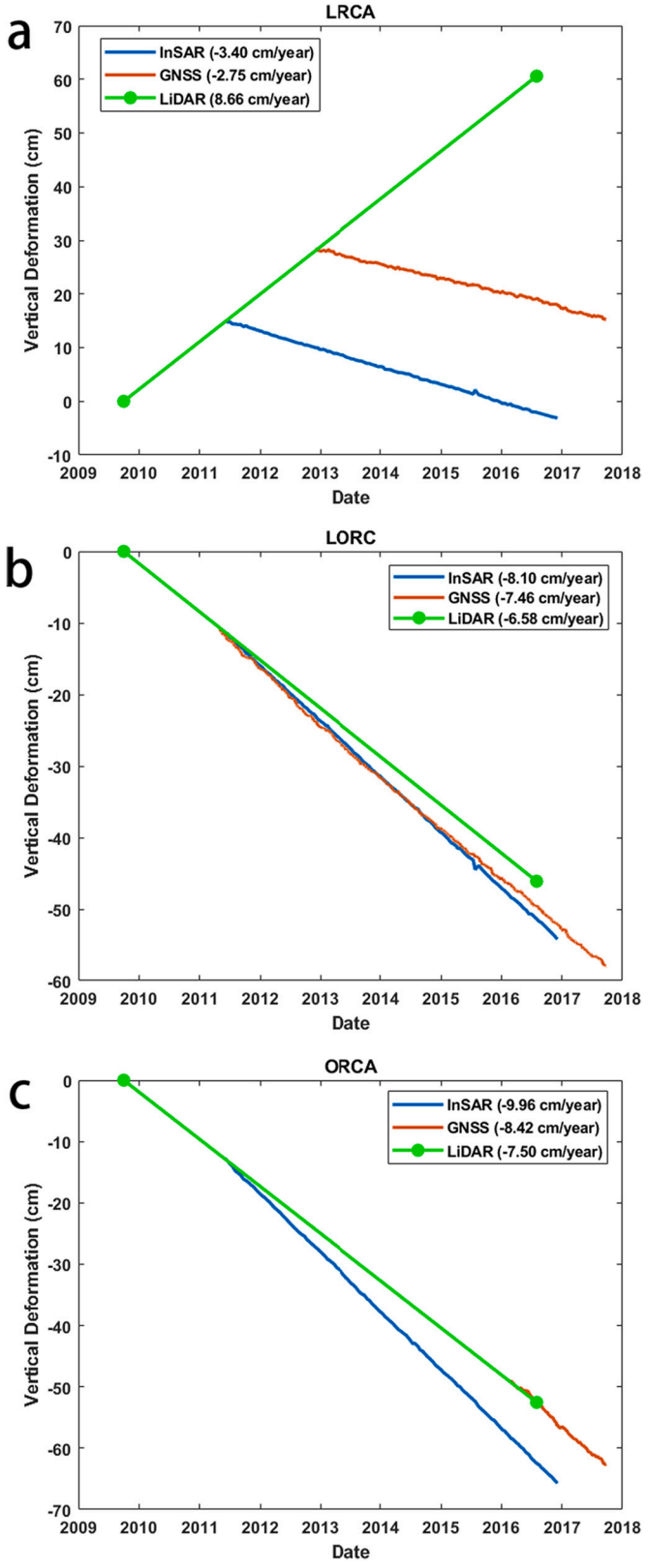

Fig. 6. InSAR, GNSS and LiDAR time series at LRCA (a), LORC (b), ORCA (c). See the location of the GNSS stations in Fig. 1.

incidence angle, but also depends on the shape of the surface of the observed object. So the position of a point within a point cloud is uncertain and complex (Soudarissanane et al., 2011). On the other hand, the registration error may be anisotropic if the distribution of registration constraints is not homogeneous, which is closely related to raw data accuracy and precision (Bae and Lichti, 2008). The registration error in the whole area could not be accurately calculated due to widespread subsidence area (Li et al., 2020). Finally, the contribution of roughness affects the calculation of the surface normal orientation, which is the least well constrained error (Lague et al., 2013).

Table 3
Statistics of the comparison between LiDAR-InSAR, LiDAR-GNSS and InSAR-GNSS results for points LORC and ORCA. See comparison in Fig. 6.

Statistics index	MD (cm/year)	MaxD (cm/year)	MinD (cm/year)	RMSE (cm/year)	MAPE (%)
LiDAR-InSAR	1.446 ± 0.598	1.869	1.024	1.507	19.746
LiDAR-GNSS	0.484 ± 0.141	0.584	0.385	0.494	6.618
InSAR-GNSS	0.615 ± 0.164	0.730	0.499	0.625	7.522

5.2. Characteristic of different technologies

Due to the different techniques of acquisition and processing, LiDAR and InSAR have their own characteristics leading to different application advantages (Table 5). The application advantages of LiDAR results are not only to monitor large-gradient deformation with less time series but also to detect rapid and small collapse movements (e.g. sinkholes). However, because of the InSAR theory, small deformations could be only extracted from points that feature stable scattering. Furthermore, InSAR displacement results are mainly feasible for Persistent Scatterers (PS) and Distributed Scatterers (DS), and unavailable over areas of low coherence, which results in uneven and sparse distribution (Even and Schulz, 2018; Perissin and Ferretti, 2007), whereas LiDAR technique provides an unstructured dense coverage. As a consequence, there are more possibilities that some sites of interest may not have coherent points nearby after InSAR processing.

With regards to the acquisition, there are both open-access and commercial datasets about LiDAR and InSAR. Commercial LiDAR datasets are usually customized and preprocessed, while there are plenty of regular commercial InSAR satellites such as CSK operated by the Italian Space Agency (ASI) or TerraSAR-X from the German Aerospace Center (DLR). Also important, the LiDAR data acquisition from aerial aircraft can be planned by the users being more flexible in the flight parameters. In contrast, open-access SAR images used for InSAR processing over wide areas are systematically acquired at regular time intervals (e.g. Sentinel-1 from the European Space Agency). Otherwise, customized InSAR and LiDAR datasets are more expensive than commercial non-customized InSAR datasets. In this case, LiDAR datasets are freely available from PNOA while InSAR datasets are acquired from commercial CSK satellites. As a consequence, it is possible to obtain displacements time series from open-access InSAR, but only cumulative deformation results from LiDAR unless regular and expensive customized flights were performed.

It should be also mentioned that, according to InSAR theory (Bekaert et al., 2015a; Hooper, 2006; Hooper et al., 2012; Hooper et al., 2007), although the accuracy of InSAR data is lower than LiDAR data, the precision of the displacement rate derived from InSAR by calculating the phase differences is higher than that obtained from LiDAR differencing. Moreover, for the time series InSAR techniques a large number of radar images are available to determine the displacement, while it is usually hard to collect enough open-access time series LiDAR datasets of the same scene.

InSAR capability to detect slow deformation over terrain areas is limited by temporal decorrelation, geometric decorrelation and atmospheric artifacts, which is also a relative advantages of LiDAR. Even decorrelation and atmospheric problems can be solved by multi-temporal InSAR, while these techniques require more machine and

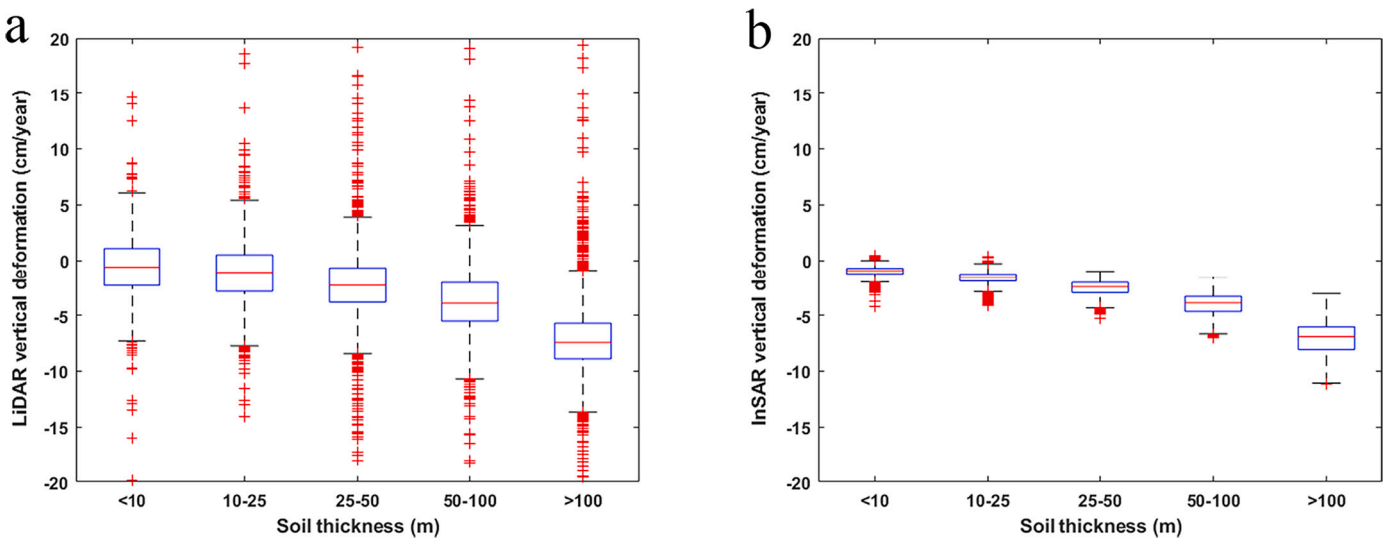

Fig. 7. Relationship between compressible soil thickness and vertical deformation rates derived from the LiDAR (a) and InSAR (b).

Table 4
Residual number and rejection rate of points after the application different of filters.

	2009 point cloud		2016 point cloud	
	N° of points	Rejection rate (%)	N° of points	Rejection rate (%)
N° of points of the original dataset	34,052,366		34,122,595	
N° of points of the classified dataset	24,860,169	26.99	22,567,743	33.86
N° of points of the classified dataset and processed by gradient	24,710,387	0.60	22,416,079	0.67
N° of points of the classified dataset and processed by gradient and CSF	22,104,544	10.55	20,036,065	10.67

Table 5
Comparison of the main features of LiDAR and InSAR for monitoring land subsidence.

Concept	LiDAR	InSAR
Application advantages	Large-gradient deformation, rapid and small collapse movements	Slow displacement
Distribution of points	Unstructured dense distribution according to sample interval	Uneven and sparse distribution according to coherent points
Acquisition	Open-access / non-customized datasets and customized datasets	Open-access datasets, commercial non-customized datasets and customized datasets
Flight parameters	Flexible for customized datasets and rigid for open-acces/non-customized datasets	Regular acquisitions
Time series sampling frequency	Low	Medium
Precision of DEM	High	Medium
Precision of velocity	Medium	High
Decorrelation	No	Temporal and geometric decorrelation
Atmospheric retardation	Low	High

skill-demanding resources than LiDAR processing.

6. Conclusions

In this work, a new advanced solution for the regional measurement of large vertical deformation caused by groundwater-withdrawal-induced land subsidence using open-access, non-specifically acquired and non-customized LiDAR datasets is presented. Its performance was tested and validated by InSAR and GNSS techniques. Moreover, the relationships between land subsidence deformation and the distribution of compressible soil thickness and aquifer system were analyzed and discussed. Finally, the sources of errors in LiDAR processing were systematically summarized, and the characteristics of the two technologies were compared. The main conclusions can be drawn as follows:

First, we took the lead to use aerial LiDAR datasets available at nation-scale in some countries to successfully monitor land subsidence. The methodology applied to the Alto Guadalentín basin, an area exhibiting the highest subsidence rate in Europe caused by groundwater withdrawal, provides a cumulative LiDAR deformation map between 2009 and 2016. The results are in agreement with previous research in this region. The deformation map indicates that vertical deformation during the period 2009–2016 was concentrated in the center of the basin, exhibiting an annual velocity up to −14 cm/year. Continuous data from GNSS stations and time series data from InSAR have confirmed the existence of that trend. These data were also used to validate the vertical deformation results obtaining a good agreement.

Second, land subsidence results were compared to the compressible soil thickness variations. A clear relationship between compressible soil thickness and land subsidence indicating that the thicker the accumulated compressible soil the larger the vertical deformations can be verified in this area in agreement with previous works (Bonì et al., 2015; Ezquerro et al., 2020).

Third, in the wake of these results, an upcoming challenge is to analyze in detail main characteristic and uncertainties of open-access LiDAR processing. The use of LiDAR has led to a complementary deformation monitoring of the Guadalentín aquifer system characterized by the even spatial coverage, flexible acquisition, and high sensitivity for changes, which is unattainable by traditional methods.

The proposed methodology opens the door to the exploitation of massive archives of LiDAR datasets to study large deformations at regional scale in different areas of interest of Spain and other countries in which similar LiDAR open-access and non-customized datasets are available. More widely, the findings of this work confirmed the

capability of LiDAR technology to monitor a variety of activities at regional scale in the framework of land subsidence mitigation and management, which has significant implications for its application in similar geological contexts.

CRediT authorship contribution statement

Liuru Hu: Conceptualization, Methodology, Data curation, Validation, Formal analysis, Writing – original draft, Resources, Writing – review & editing, Supervision. **María I. Navarro-Hernández:** Validation, Formal analysis, Supervision. **Xiaojie Liu:** Formal analysis, Supervision. **Roberto Tomás:** Conceptualization, Methodology, Data curation, Formal analysis, Writing – original draft, Resources, Writing – review & editing, Supervision, Funding acquisition. **Xinming Tang:** Data curation, Writing – original draft, Supervision, Funding acquisition. **Guadalupe Bru:** Validation, Supervision. **Pablo Ezquerro:** Validation, Writing – review & editing, Supervision. **Qingtao Zhang:** Writing – review & editing, Supervision.

Declaration of Competing Interest

The authors declare that they have no known competing financial interests or personal relationships that could have appeared to influence the work reported in this paper.

Data availability

Data will be made available on request.

Acknowledgments

This research was funded by the ESA-MOST China DRAGON-5 project (ref. 59339) and by a Chinese Scholarship Council studentship awarded to Liuru Hu (Ref. 202004180062). María I. Navarro-Hernández and Guadalupe Bru are funded by the PRIMA programme supported by the European Union under grant agreement No 1924, project RESERVOIR. The LiDAR data and orthophotos used in this work were freely provided by the Centro Nacional de Información Geográfica (CNIG) del Instituto Geográfico Nacional (IGN) de España (https://www.cnig.es/). The authors would like to thank Jesús María Garrido Sáenz de Tejada and Antonio de la Torre Morales from the Instituto Geográfico Nacional (IGN) of Spain for providing the altimetric precision control information of the LiDAR datasets used in this work.

Appendix A. Supplementary data

Supplementary data to this article can be found online at https://doi.org/10.1016/j.rse.2022.113218.

References

Amighpey, M., Arabi, S., 2016. Studying Land Subsidence in Yazd Province, Iran, by Integration of InSAR and Levelling Measurements, 4. Remote Sensing Applications: Society and Environment.

ArcGIS, 2022. How To: Extract LAS ground points from a LAS dataset to a TIN-based surface in ArcMap. https://support.esri.com/en/technical-article/000021888.

Bae, K.-H., Lichti, D.D., 2008. A method for automated registration of unorganised point clouds. ISPRS J. Photogramm. Remote Sens. 63 (1), 36–54.

Balasubramaniam, A.S., Brenner, R.P., 1981. Chapter 7 - consolidation and settlement of soft clay, developments in geotechnical engineering. Elsevier 479–566.

Béjar-Pizarro, M., Guardiola-Albert, C., García-Cárdenas, R.P., Herrera, G., Barra, A., López Molina, A., Tessitore, S., Staller, A., Ortega-Becerril, J.A., García-García, R.P., 2016. Interpolation of GPS and geological data using InSAR deformation maps: method and application to land subsidence in the alto Guadalentín aquifer (SE Spain). Remote Sens. 8 (11).

Bekaert, D., Hooper, A., Wright, T., 2015a. A spatially-variable power-law tropospheric correction technique for InSAR data. Journal of geophysical research: solid. Earth 120.

Bekaert, D., Walters, R., Wright, T., Hooper, A., Parker, D., 2015b. Statistical comparison of InSAR tropospheric correction techniques. Remote Sens. Environ. 170, 40–47.

Bernard, T., Lague, D., Steer, P., 2021. Beyond 2D landslide inventories and their rollover: synoptic 3D inventories and volume from repeat lidar data. Earth Surface Dynamics 9, 1013–1044.

Blanco-Sánchez, P., Mallorquí, J.J., Duque, S., Monells, D., 2008. The coherent pixels technique (CPT): an advanced DInSAR technique for nonlinear deformation monitoring. Pure Appl. Geophys. 165 (6), 1167–1193.

Bonì, R., Herrera, G., Meisina, C., Notti, D., Béjar-Pizarro, M., Zucca, F., González, P.J., Palano, M., Tomás, R., Fernández, J., Fernández-Merodo, J.A., Mulas, J., Aragón, R., Guardiola-Albert, C., Mora, O., 2015. Twenty-year advanced DInSAR analysis of severe land subsidence: the alto Guadalentín Basin (Spain) case study. Eng. Geol. 198, 40–52.

Borsa, A., Minster, B., 2012. Rapid determination of near-fault earthquake deformation using differential LiDAR. Bull. Seismol. Soc. Am. 102, 1335–1347.

Brock, J., Sallenger, A., Krabill, W.B., Swift, R., Wright, C., 2001. Recognition of fiducial surfaces in Lidar surveys of coastal topography. Photogramm. Eng. Remote. Sens. 67, 1245–1258.

Bull, J., Miller, H., Gravley, D.M., Costello, D., Hikuroa, D., Dix, J., 2010. Assessing debris flows using LIDAR differencing: 18 may 2005 Matata event, New Zealand. Geomorphology 124, 75–84.

Cai, S., Zhang, W., Liang, X., Peng, W., Qi, J., Yu, S., Yan, G., Shao, J., 2019. Filtering airborne LiDAR data through complementary cloth simulation and progressive TIN densification filters. Remote Sens. 11, 1037.

Castellazzi, P., Arroyo, N., Martel, R., Calderhead, A., Normand, C.L., Garfias, J., Rivera, A., 2016. Land subsidence in major cities of Central Mexico: interpreting InSAR-derived land subsidence mapping with hydrogeological data. Int. J. Appl. Earth Obs. Geoinf. 47, 102–111.

Cerón García, J.C., 1995. Estudio hidrogeoquímico del acuífero del alto guadalentín (Murcia). info:eu-repo/semantics/doctoralThesis Thesis. Universidad de Granada.

Cerón, J., Pulido, A., 1996. Groundwater problems resulting from CO2 pollution and overexploitation in alto Guadalentín aquifer (Murcia, Spain). Environ. Geol. 28, 223–228.

Chen, C., Li, Y., Li, W., Dai, H., 2013. A multiresolution hierarchical classification algorithm for filtering airborne LiDAR data. ISPRS J. Photogramm. Remote Sens. 82, 1–9.

Chen, C., Guo, J., Wu, H., Li, Y., Shi, B., 2021. Performance comparison of filtering algorithms for high-density airborne LiDAR point clouds over complex LandScapes. Remote Sens. 13, 2663.

CHS, 2006. Plan especial ante situaciones de alerta y eventual sequía en la cuenca del Segura: 238 Confederación hidrográfica del Segura. Confederacion Hidrografica del Segura, Murcia.

CNIG, 2022. DIGITAL ELEVATION MODELS. https://centrodedescargas.cnig.es/CentroDescargas/locale?request_locale=en.

Dach, R., Andritsch, F., Arnold, D., Bertone, S., Fridez, P., Jäggi, A., Jean, Y., Maier, A., Mervart, L., Meyer, U., Orliac, E., Geist, E., Prange, L., Scaramuzza, S., Schaer, S., Sidorov, D., Susnik, A., Villiger, A., Walser, P., Thaller, D., 2015. Bernese GNSS Software Version 5.2.

De Winter, J., Gosling, S., Potter, J., 2016. Comparing the Pearson and Spearman correlation coefficients across distributions and sample sizes: a tutorial using simulations and empirical data. Psychol. Methods 21, 273–290.

Deng, X., Guo, T., Qingyang, W., 2021. A novel fast classification filtering algorithm for LiDAR point clouds based on small grid density clustering. Geodesy and Geodynamics 13.

Even, M., Schulz, K., 2018. InSAR deformation analysis with distributed Scatterers: a review complemented by new advances. Remote Sens. 10 (5).

Ezquerro, P., Guardiola-Albert, C., Herrera, G., Fernández-Merodo, J.A., Béjar-Pizarro, M., Bonì, R., 2017. Groundwater and subsidence modeling combining geological and multi-satellite SAR data over the alto Guadalentín aquifer (SE Spain). Geofluids 2017, 1359325.

Ezquerro, P., Tomás, R., Béjar-Pizarro, M., Fernández-Merodo, J.A., Guardiola-Albert, C., Staller, A., Sánchez-Sobrino, J.A., Herrera, G., 2020. Improving multi-technique monitoring using Sentinel-1 and Cosmo-SkyMed data and upgrading groundwater model capabilities. Sci. Total Environ. 703, 134757.

Fernandez, J., Prieto, J., Escayo, J., Camacho, A., Luzon, F., Tiampo, K., Palano, M., Abajo, T., Pérez-Martín, E., Velasco-Gómez, J., Herrero-Tejedor, T., Bru, G., Molina, I., Herrera, J., Rodriguez, G., Gómez, I., Mallorqui, J., 2018. Modeling the two- and three-dimensional displacement field in Lorca, Spain, subsidence and the global implications. Sci. Rep. 8.

Fernández-Merodo, J.A., Ezquerro, P., Manzanal, D., Béjar-Pizarro, M., Mateos, R.M., Guardiola-Albert, C., García-Davalillo, J.C., López-Vinielles, J., Sarro, R., Bru, G., Mulas, J., Aragón, R., Reyes-Carmona, C., Mira, P., Pastor, M., Herrera, G., 2021. Modeling historical subsidence due to groundwater withdrawal in the alto Guadalentín aquifer-system (Spain). Eng. Geol. 283, 105998.

Galloway, D., Hoffmann, J., 2007. The application of satellite differential SAR interferometry-derived ground displacements in hydrogeology. Hydrogeol. J. 15.

Ge, L., Ng, A., Li, X., Abidin, H.Z., Gumilar, I., 2014. Land subsidence characteristtics of Bandung Basin as revealed by ENVISAT ASAR and ALOS PALSAR interferometry. Remote Sens. Environ. 154, 46–60.

GeaMap, 2022. Aerial orthophoto viewer of Spain in different years. https://www.geamap.com/es/ortofoto-espana.

González, P., Fernandez, J., 2011. Drought-driven transient aquifer compaction imaged using multitemporal satellite radar interferometry. Geology 39, 551–554.

González, P.J., Fernández, J., 2011. Drought-driven transient aquifer compaction imaged using multitemporal satellite radar interferometry. Geology 39 (6), 551–554.

He, Y., Xu, G., Kaufmann, H., Wang, J., Ma, H., Liu, T., 2021. Integration of InSAR and LiDAR Technologies for a Detailed Urban Subsidence and Hazard Assessment in Shenzhen, China. Remote Sensing 13, 2366.

Hooper, A., 2006. Persistent Scatter Radar Interferometry for Crustal Deformation Studies and Modeling of Volcanic Deformation.
Hooper, A., Segall, P., Zebker, H.A., 2007. Persistent scatterer InSAR for crustal deformation analysis, with application to Volcán Alcedo, Galápagos. J. Geophys. Res. 112.
Hooper, A., Bekaert, D., Spaans, K., Arikan, M., 2012. Recent advances in SAR interferometry time series analysis for measuring crustal deformation. Tectonophysics 514.
Hu, B., Chen, J., Zhang, X., 2019. Monitoring the land subsidence area in a coastal urban area with InSAR and GNSS. Sensors 19, 3181.
IGME, 1981. Mapa Geológico de España, 1:50.000, Sheet Lorca (953). Tech. Rep. Servicio de Publicaciones Ministerio de Industria, Madrid, Spain.
IGN, 2009. Altimetric Precision Control Information of the ALS Campaign Performed in 2009. Instituto Geográfico Nacional, Internal Report.
IGN, 2016. Altimetric Precision Control Information of the ALS Campaign Performed in 2016. Instituto Geográfico Nacional, Internal Report.
IGN, 2022. Plan Nacional de Ortografía Aérea (PNOA). https://pnoa.ign.es/estado-del-proyecto-lidar.
Imakiire, T., Koarai, M., 2012. Wide-area land subsidence caused by "the 2011 off the Pacific coast of Tohoku earthquake". Soils Found. 52, 842–855.
Khan, S., Huang, Z., Karacay, A., 2014. Study of ground subsidence in Northwest Harris county using GPS, LiDAR, and InSAR techniques. Nat. Hazards 73, 1143–1173.
Koning, M., Haasnoot, J., Buuren, R., Weijland, M., Bisschop, C., 2020. Determination of amount of land subsidence based on INSAR and LiDAR monitoring for a dike strengthening project. Proceedings of the International Association of Hydrological Sciences 382, 57–62.
Lague, D., Brodu, N., Leroux, J., 2013. Accurate 3D comparison of complex topography with terrestrial laser scanner: application to the Rangitikei canyon (N-Z). ISPRS J. Photogramm. Remote Sens. 82.
Latypov, D., 2002. Estimating relative lidar accuracy information from overlapping flight lines. ISPRS J. Photogramm. Remote Sens. 56 (4), 236–245.
Li, Y., 2013. Filtering airborne LIDAR data by an improved morphological method based on multi-gradient analysis. ISPRS - international archives of the photogrammetry, remote sensing and spatial. Inf. Sci. XL-1/W1, 191–194.
Li, Y., Yong, B., Oosterom, P., Lemmens, M., Wu, H., Ren, L., Zheng, M., Zhou, J., 2017. Airborne LiDAR data filtering based on geodesic transformations of mathematical morphology. Remote Sens. 9, 1104.
Li, P., Wang, R., Wang, Y., Tao, W., 2020. Evaluation of the ICP Algorithm in 3D Point Cloud Registration. IEEE Access, PP, p. 1.
Martinez-Diaz, J., Bejar, M., Álvarez-Gómez, J., Mancilla, F.D.L., Stich, D., Herrera, G., Morales, J., 2012. Tectonic and seismic implications of an intersegment rupture: the damaging may 11th 2011 mw 5.2 Lorca, Spain, earthquake. Tectonophysics 546–547, 28–37.
Monterroso Checa, A., 2017. Remote sensing and archaeology from Spanish LiDAR-PNOA: identifying the amphitheatre of the roman city of torreparedones (Córdoba-Andalucía-Spain). Mediter. Archaeol. Archaeom. 17, 15–22.
Perissin, D., Ferretti, A., 2007. Urban-target recognition by means of repeated Spaceborne SAR images. IEEE Trans. Geosci. Remote Sens. 45 (12), 4043–4058.
Rigo, A., Bejar, M., Martinez-Diaz, J., 2013. Monitoring of Guadalent'in valley (southern Spain) through a fast SAR interferometry method. J. Appl. Geophys. 91.
Sansosti, E., Berardino, P., Bonano, M., Calò, F., Castaldo, R., Casu, F., Manunta, M., Manzo, M., Pepe, A., Pepe, S., Solaro, G., Tizzani, P., Zeni, G., Lanari, R., 2014. How second generation SAR systems are impacting the analysis of ground deformation. Int. J. Appl. Earth Obs. Geoinf. 28, 1–11.
Scott, C., Champenois, J., Klinger, Y., Nissen, E., Maruyama, T., Chiba, T., Arrowsmith, R., 2019. 2016 M7 Kumamoto, Japan, earthquake slip field derived from a joint inversion of differential Lidar topography, optical correlation, and InSAR surface displacements. Geophys. Res. Lett. 46.
Scott, C., Phan, M., Nandigam, V., Crosby, C., Arrowsmith, R., 2021. Measuring change at Earth's surface: on-demand vertical and three- dimensional topographic differencing implemented in OpenTopography. Geosphere 17.
Silva, P.G., 2014. The Guadalentín Tectonic Depression. Betic Cordillera, Murcia, pp. 25–35.
Soudarissanane, S., Lindenbergh, R., Menenti, M., Teunissen, P., 2011. Scanning geometry: influencing factor on the quality of terrestrial laser scanning points. ISPRS J. Photogramm. Remote Sens. 66 (4), 389–399.
Tomás, R., Márquez, Y., Lopez-Sanchez, J., Delgado, J., Blanco, P., Mallorqui, J., Martínez, M., Herrera, G., Mulas, J., 2005. Mapping ground subsidence induced by aquifer overexploitation using advanced differential SAR interferometry: Vega Media of the Segura River (SE Spain) case study. Remote Sens. Environ. 269–283.
Tomás, R., Romero, R., Mulas, J., Marturia, J., Mallorqui, J., Lopez-Sanchez, J., Herrera, G., González, P., Fernandez, J., Duque, S., Concha-Dimas, A., Cooksley, G., Castañeda, C., Carrasco, D., Blanco, P., 2013. Radar interferometry techniques for the study of ground subsidence phenomena: a review of practical issues through cases in Spain. Environ. Earth Sci. 71.
Vajedian, S., Motagh, M., Nilfouroushan, F., 2015. StaMPS improvement for deformation analysis in mountainous regions: implications for the Damavand volcano and Mosha fault in Alborz. Remote Sens. 7, 8323–8347.
Wang, X., Li, Y., Peng, Y., Ying, S., 2020. A Coarse-to-Fine Generalized-ICP Algorithm with Trimmed Strategy. IEEE Access, p. 1.
Xiao, R., Yu, C., Li, Z., He, X., 2021. Statistical assessment metrics for InSAR atmospheric correction: applications to generic atmospheric correction online service for InSAR (GACOS) in eastern China. Int. J. Appl. Earth Obs. Geoinf. 96, 102289.
Yousefi, R., Talebbeydokhti, N., 2021. Subsidence Monitoring by Integration of Time Series Analysis from Different SAR Images and Impact Assessment of Stress and Aquitard Thickness on Subsidence in Tehran. Environmental Earth Sciences, Iran, p. 80.
Zhang, Y., Xiong, X., Zheng, M., Huang, X., 2015. LiDAR strip adjustment using multifeatures matched with aerial images. IEEE Trans. Geosci. Remote Sens. 53 (2), 976–987.
Zhang, W., Qi, J., Peng, W., Wang, H., Xie, D., Wang, X., Yan, G., 2016. An easy-to-use airborne LiDAR data filtering method based on cloth simulation. Remote Sens. 8, 501.